Room-temperature multi-beam, multi-wavelength bound state in the continuum laser

Son Tung Ha,[†,§] Ramón Paniagua-Domínguez,[†,§] Arseniy I. Kuznetsov[†,*]

[†]Institute of Materials Research and Engineering, A*STAR (Agency for Science, Technology and Research), Singapore 138634

*Corresponding author: arseniy_kuznetsov@imre.a-star.edu.sg

[§]These authors contributed equally to this work.

ABSTRACT: We report a highly polarized multi-beam, multi-wavelength III-V semiconductor laser based on the concept of bound states in the continuum (BIC). By utilizing destructive interferences of guided-mode resonances in an active slab supported by a grating structure, we create both symmetry-protected and accidental BIC resonances within the gain spectrum of InGaP multi-quantum wells and achieve lasing in these modes simultaneously. Well defined multi-lasing beams at different wavelengths (i.e., 664.9 nm @ 0.2°, 656.4 nm @ 2.5°, 646.4 nm @ 5.1°, and 636.7 nm @ 7.6°) with transverse magnetic polarization can be obtained in a single device operating at room temperature. Furthermore, the lasing wavelengths can be precisely tuned by changing the grating parameters. The laser concept presented in this paper is promising for applications in highly directional surface-emitting lasers, optical communications, bio-sensing and signal processing.

KEYWORDS: Bound states in the continuum, guided resonance, III-V semiconductor device, surface-emitting laser, multi-beam laser.

Miniaturized semiconductor lasers with controllable directionality and wavelength tunability are highly desirable for applications in integrated photonics, on-chip light sources, optical communications, signal processing, bio-sensing and advanced display technologies[1–11]. Two of the most commonly used semiconductor lasers are vertical-cavity surface-emitting lasers (VCSEL) based on distributed Bragg reflectors (DBR) and distributed feedback (DFB) lasers based on multiple reflections from diffraction gratings. Even though these laser cavities are highly successful in the industry, there are several drawbacks: low polarization selectivity, difficulty to control directionality, and large laser footprint. Beam engineering of laser devices has been a long-lasting effort of the community to create a light source with enhanced performance and new functionalities[12–17]. These devices can then be used in multiple optoelectronic applications without the need for external optical components. However, up to now, there is no laser cavity that can support multiple modes with different beam directions in a single device. Typically, additional optical components are needed to separate the multi-mode lasing signal, such as a grating structure on top of a surface-emitting laser cavity[18]. Such integration not only increases the complexity of the manufacturing process but also reduces the beam intensity and quality.

Bound state in the continuum has recently become an intriguing concept to design laser cavities[19–21]. Its feedback mechanism has enabled highly directional, miniaturized, high power, and low threshold micro/nano lasers. BICs are peculiar radiation-less states that remain spatially localized (hence the term "bound") with an infinite lifetime even though they reside in the radiation continuum[21–29]. Taking advantage of its naturally high-quality factor, multiple laser devices have been demonstrated in the last few years based on the concept of BIC resonance[15,30–39]. However, most of them focus on a single BIC mode, resulting in single wavelength, single-mode laser devices, with a few exceptions[40,41]. In general, BICs in two-dimensional periodic structures can be classified into two categories: symmetry-protected BICs, which happen at the Γ point of the band structure, and accidental BICs, which happen at oblique angles to the normal. In this work, we utilize the two types of BIC modes in a single resonant structure to create a multi-beam, multi-wavelength laser device capable of producing multiple well-defined lasing beams at different wavelengths.

Figure 1a illustrates the design concept of our laser device, in which a grating structure is fabricated on top of a slab containing an active gain medium layer. The grating structure is designed to support multiple guided modes within the slab at the emission spectrum of the gain medium. In this case, BICs can be formed by total destructive interferences between counter-propagating guided modes with the same amplitude and opposite phases[35,42–44]. The total destructive interferences can either happen at the normal incidence by the same order or at an oblique angle by different order guided modes. By controlling the geometrical parameters, such as the slab thickness and the grating period, either a single mode or a multi-mode laser cavity can be designed.

To demonstrate the design concept experimentally, we chose GaP as the material platform to fabricate our laser devices. We do so because of its high refractive index of ~ 3.5 and absorption-less character at its emission wavelength, located in the red portion of the visible spectrum. The wafer was epitaxially grown in a light-emitting diode configuration using metal-organic chemical vapour deposition (MOCVD) by ChangeLight co. ltd. (Xianmen, China). The wafer structure consists of p-AlGaInP (~100nm), InGaP/InAlGaP MQWs (~180 nm) and n-AlInP (~600 nm) on a GaAs wafer, which was then transferred onto a Ge (20nm)/Au(200nm)/Si substrate by a standard wafer bonding process (see supplementary Fig. S1, Table S2, and Fig. S3 for a cross-section Scanning electron microscope (SEM) image, elemental composition analysis, and Raman spectroscopy analysis of the wafer, respectively). It is noted that the Ge/Au layer act as a bottom mirror to support the guided modes within the slab. Without the metal layer, the guided modes may leak to the substrate, and the BIC modes become quasi-BICs, as discussed by Z. F. Sadrieva et al.[45] The grating structure is patterned by an e-beam lithography (EBL) process using hydrogen silsesquioxane (HSQ) as a negative resist. The structure is then transferred to the n-AlInP layer by reactive ion etching (RIE) with chlorine chemistry at an elevated temperature (see Methods and supplementary Fig. S4 for the detailed fabrication process). We keep a fixed gap = 100 nm and an array size of ~50 × 50 μm^2 for the grating structures in all laser devices presented in this work. Thus, for a device with a grating beam width of W = 90 nm, its grating period will be P = 190 nm. SEM images of a typical laser device are shown in Fig. 1b & c.

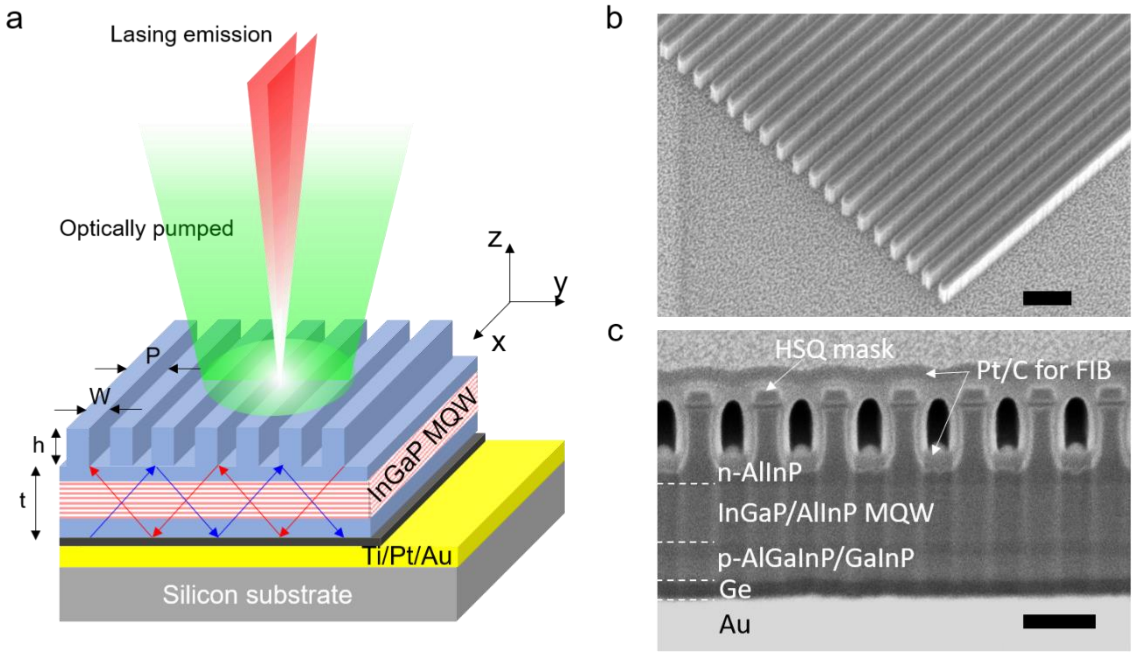

Figure 1. (a) Design concept of the surface-emitting laser based on BICs formed by the destructive interference of counter-propagating guided-mode resonances inside a slab consisting of a gain medium. (b) SEM image of the fabricated grating structure. (c) Cross-section SEM image of the laser device showing different device layers. Scale bars in (b) and (c) are 200 nm.

To characterize the optical properties of the fabricated devices, we used a home-built back focal plane (BFP) micro-spectrometer setup[36] (see Methods for the measurement details). The sample is oriented on the microscope stage such that the grating beam direction (i.e., x-axis) is projected perpendicular onto the spectrograph slit (y-axis), which is the angle-resolved direction in the BFP measurements. Figure 2a,b show the angle-resolved reflection spectra of a device with the slab thickness t = 300 nm, grating height h = 250nm, and grating beam width W = 90 nm (i.e., P = 190 nm) with excitation polarization perpendicular to the slit (TE) and parallel to the slit (TM), respectively (see supplementary Fig. S5 & S6 for reflection spectra of the slab and other devices with different grating beam widths). Figure 2c,d show the simulated reflection spectra for the same device indicating good agreement with the experimental measurements. For this device, the first order guided-mode resonance at the normal incident is designed to be around 620 nm which is the peak of the gain spectrum of InGaP MQWs. At the normal incidence, due to the destructive and constructive interferences of the counter-propagating guided modes, the constructive band will become bright mode, normally referred to as diffraction-couple band-edge mode, while the destructive one will become dark mode, also known as a bound state in the continuum. These modes have been extensively studied by D. A. Bykov et al.[44] using a coupled-wave model and numerical analysis. In this case, the high-quality factor nature of the BIC mode can be utilized for lasing generation if a proper gain medium is overlapped with these modes. Figure 2e,f show the mode profiles of the first order symmetry-protected BIC modes for both TE and TM excitation, respectively. We can see that the mode profiles are well-positioned to overlap with the InGaP/AlInP MQWs as can be seen from the SEM image of the sample in Figure 1c. Figure 2g,h show the angle-resolved photoluminescence (PL) of the slab itself (g) and the slab with the grating structure (h) (see supplementary Fig. S7 for PL spectra of the devices with other grating parameters). The results show that, with the presence of the grating structure, the PL of the MQWs is strongly coupled to the first order guided-mode resonances. By further analysing the PL and reflection spectra shown in Figure 2i, we can see that the PL is mostly coupled to the TM rather than TE guided mode. This can be explained by the better spatial overlapping of the TM mode with the MQW layers comparing to the TE mode (see Figure 1c, 2c, & 2f). This high selectivity of polarization coupling gives us a way to generate a highly polarized lasing beam, which will be discussed in the following parts.

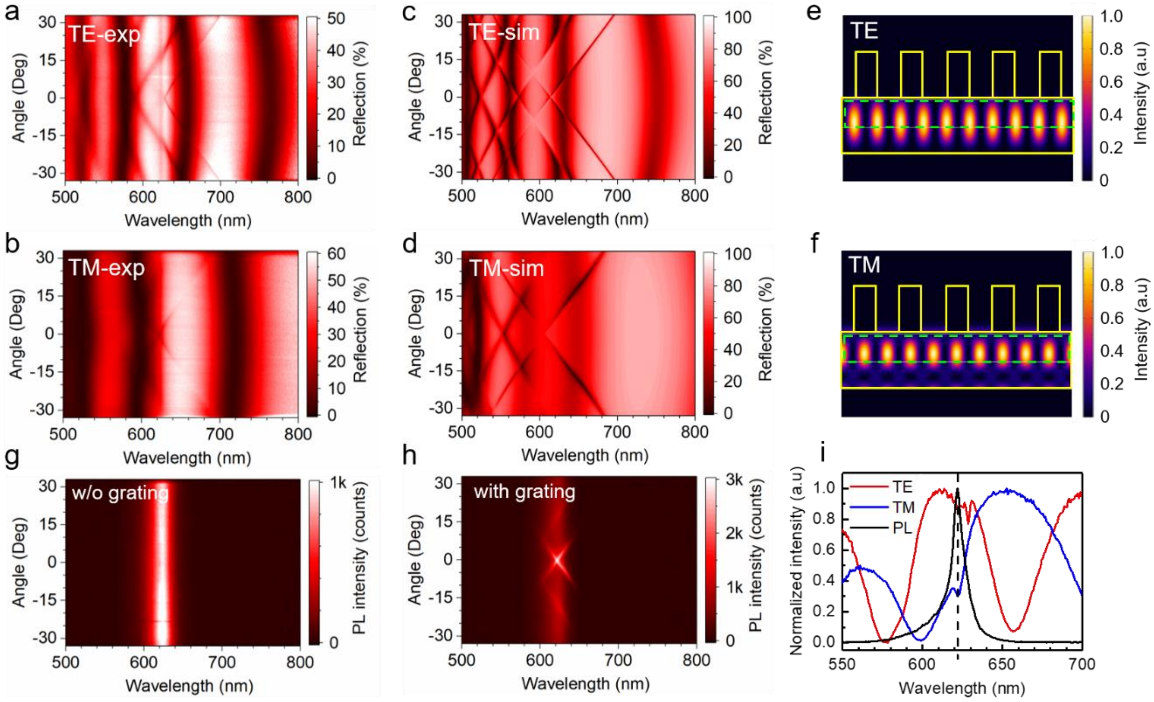

Figure 2. (a, b) Measured angle-resolved reflection spectra for TE and TM excitation, respectively, of a lasing device with the grating beam width W = 90 nm (i.e., P = 190 nm), and the slab thickness t = 300 nm. (c, d) Simulated angle-resolved reflection spectra of the device for TE and TM excitation, respectively. (e, f) Field distribution of the first order symmetry-protected BIC mode for TE and TM excitation, respectively. (g, h) PL spectra of the device areas without and with the grating structure, respectively. (i) Reflection and PL spectra near 0° angle extracted from (a), (b), & (h) showing the coupling of PL to the TM mode rather than TE mode.

To obtain lasing, we optically excited the device using a femtosecond (fs) laser at 530 nm wavelength with a pulse width of 200 fs, and a repetition rate of 20 kHz at ambient conditions. The diameter of the circular laser spot is about 50 μm, which covers most of the laser device (~ 50 × 50 μm^2). The lasing results for the device are shown in Figure 3. Figure 3a shows the evolution of the photoluminescence spectra collected at ~0.2° off normal when increasing the pumping fluence from 100 to 160 μJ/cm^2. We can see that above 120 μJ/cm^2, a pronounced, sharp peak at 621 nm wavelength appears, indicating stimulated emission in the device. Further increasing pumping fluences and analysing the laser input-output dependence, we can clearly see a threshold-like behaviour, as shown in the right inset to Figure 3a, indicating that lasing action has been achieved with a lasing threshold of ~150 μJ/cm^2. By analyzing the lasing spectrum, a quality factor can be calculated by dividing the emission peak wavelength by its full width of half maximum (fwhm), which is about 2070 as shown in the left inset to Figure 3a. Figure 3b and c show the angle-resolved PL spectra of the device below (b) and above (c) lasing threshold, respectively. We can see that the lasing happens near the cross-section of the first order guided modes, as discussed above. It is noted that the lasing emission is peaked at around ±0.2° off normal (inset to Figure 3c) rather than at exactly the normal direction. This indeed reveals the symmetry-protected BIC nature of the lasing mode, which prohibits radiation outcoupling at 0°. Chen, Z. *et al*. have recently analyzed the far field pattern (FFP) of the symmetry protected BIC in a finite array using coupled wave theory[46]. Following the notation of the reference, discretization of the momentum space induced by the finite size of the PhC would give an integer increment in k-space of $\delta_k = \pi/L$, with L = 50um. Then, the FFP peak will be given by the k-vector of the envelop function $\tilde{k}_x \sim p\pi/L$, which, considering that the mode would be the 1st one (p=1), gives $\tilde{k}_x \sim \frac{p\pi}{L} = 0.0621k_0$, which in turns gives a FFP maximum of $\theta_{max} \sim \arctan\left(\frac{\tilde{k}_x}{k_0}\right) = 0.3\,°$, indeed in reasonable agreement with our experiment results.

Interestingly, we only observe the characteristic behaviour of the BIC mode in the angle-resolved lasing spectra (i.e., when the lasing mode is greatly enhanced) rather than in reflection or PL below the lasing threshold. This happens because of the spectrally close proximity of the other bright and dark modes (the latter being of the opposite polarization) and low spectral resolution of our micro spectrometer setup (~ 1.5 nm at 150 lines/mm grating). It is important to note that we achieved lasing from a symmetry-protected BIC mode rather than the diffraction-coupled band-edge mode (a.k.a. bright mode) claimed to be responsible for lasing in other periodic structures in the literature[47–50]. Figure 3d and e show the BFP images of the device PL below (d) and above (e) lasing threshold, respectively. It can be seen that the two lasing beams are elongated along the grating beam orientation. This is because the guided mode BIC in the slab is only supported in the waveguiding direction, which is perpendicular to the grating. Thus, the light is confined within this direction and is free to diffuse to higher k vectors in the other direction (i.e., k_x). Figure 3f shows the photoluminescence image of the device below and above the lasing threshold, indicating that a strong, surface-emitting lasing was achieved. Figure 3g shows the lasing spectra collected under TE and TM polarization. The result shows that the TM emission intensity is three orders of magnitude higher than the TE one, demonstrating a very high polarization degree of the laser device. More detailed analysis on the polarization dependence of the lasing emission is presented in Supplementary Information, Fig. S8.

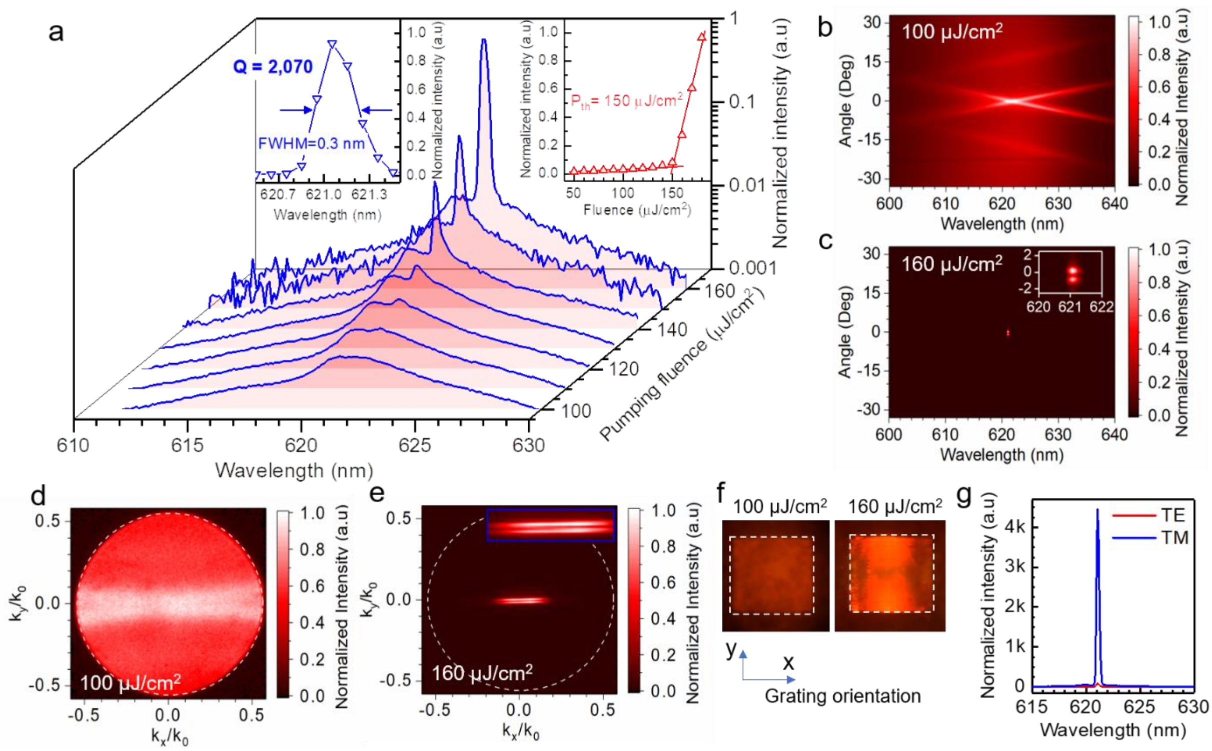

Figure 3. (a) Photoluminescence spectra evolution with increased pumping fluence showing the appearance of a narrow peak at 621 nm. Left inset: Zoom-in spectrum of the narrow lasing peak, showing a fwhm of ~ 0.3 nm, corresponding to a Q factor of 2070. Right inset: Integrated PL intensity with increasing pumping fluence showing a lasing threshold of ~ 150 μJ/cm^2. (b), (c) Angle-resolved PL spectra below (b) and above (c) lasing threshold. (d), (e) BFP images of PL below (d) and above (e) lasing threshold. (f) PL image of the lasing device below (left) and above (right) lasing threshold. (g) Lasing spectra collected at 0.2° under TE and TM polarizations.

Achieving a precise tunability of the emission wavelength is essential for any laser cavity, especially for applications in biosensing, optical communications and signal processing. In our laser devices, the BIC mode can be easily tuned by changing the grating period while keeping a constant slab thickness. Figure 4 a,b and c,d show the angle-resolved PL spectra below (a, c) and above (b, d) lasing threshold for laser devices with the same slab thickness t = 300 nm and grating beam widths W = 80 nm and W = 95 nm, respectively. We can see that a similar lasing behaviour for the symmetry-protected BIC can be obtained. The lasing spectra at 0.2° angle are shown in Figure 4e for three different device parameters. By plotting the position of the BIC as a function of the grating beam width for devices with W ranging from 70 to 150 nm (see supplementary Fig. S6 for the TM reflection spectra of these devices), we can see that the cavity resonance can be linearly shifted with a very high precision (namely, ~ 2.2 nm per 1 nm change in the grating period). This is shown in Figure 4f. In this work, since the gain spectrum of InGaP MQWs can only cover a fraction of this tunability wavelength range, we can only achieve lasing in devices with grating widths from 80 to 95 nm. By looking at the lasing threshold of these devices, we can see that the sample with a grating width of 90 nm exhibits the lowest lasing threshold, as it has the best spectral overlap between the BIC (i.e., ~621 nm) and the gain peak (i.e., ~ 620 nm).

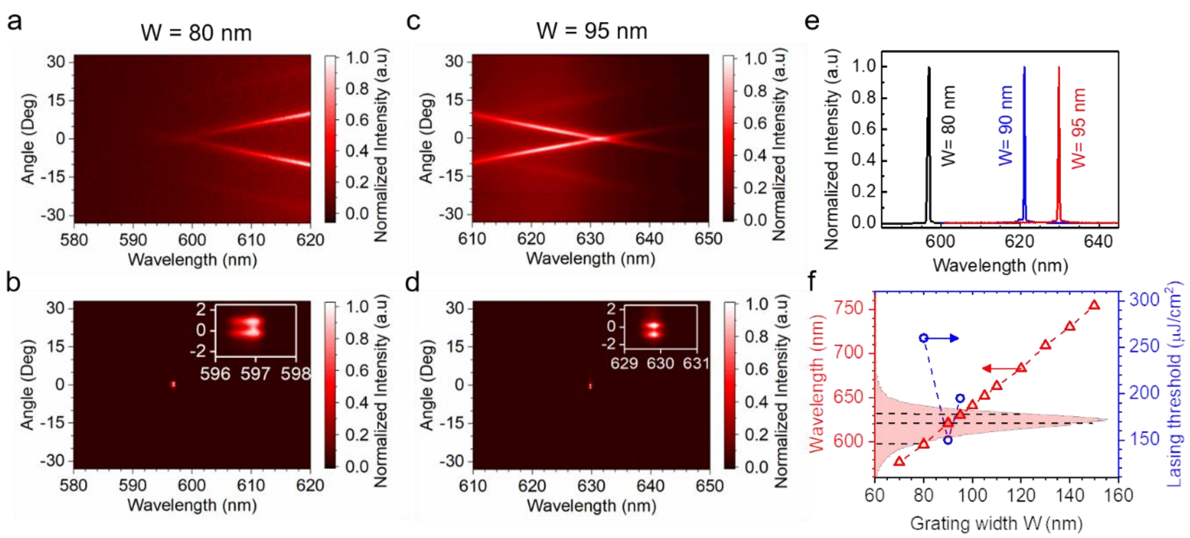

Figure 4. (a - d) Angle-resolved PL spectra below (a, c) and above (b, d) lasing threshold for arrays with W = 80 nm and W = 95 nm, respectively. (e) Lasing spectra for three arrays showing wavelength tunability within the gain spectrum. (f) BIC wavelength for different devices with grating beam widths ranging from 70 – 150 nm. We only observed lasing in three devices with W = 80, 90, 95 nm whose BIC resonances are best overlapped within the gain spectrum (pink shaded spectrum) of InGaP MQWs. For these devices, the lasing threshold is indicated by blue circles in the same plot.

Guided mode BICs can be formed not only by the destructive interference between counter-propagating guided modes of the same order, but also by counter-propagating guided modes of different orders. In the latter case, the BIC will be formed at an oblique angle, rather than at the normal one[41] creating a state known as accidental BIC. In order to achieve multi-beam lasing simultaneously, one can bring these different types of BICs spectrally closer to each other, such that they coexist within the gain spectrum of the InGaP MQWs. One way to do that is to increase the slab thickness to support higher-order guided-mode resonances. Figure 5 shows the lasing data of a device with a slab thickness t = 570 nm, grating height h = 250 nm and grating beam width W = 110 nm (P = 210 nm). With these parameters, the system can support four guided-mode BICs within the gain spectrum of InGaP MQWs, with wavelengths ranging from 635 to 665 nm. Figure 5a, b show, respectively, the measured and simulated angle-resolved reflection spectra of this laser device for TM excitation (see supplementary Fig. S9 for the measured and simulated reflection spectra for TE excitation and Fig. S10, S11 for the measured reflection spectra of devices with different grating widths under TE and TM excitation, respectively). The data shows that the first-order forward guided mode can undergo a destructive interference with: (i) the first-order backward guided mode, forming a symmetry-protected BIC, and (ii) higher-order backward guided modes, forming accidental BICs. Figure 5c,d shows the mode profiles of the symmetry-protected BIC and one of the accidental BIC, which are partially overlapped with the InGaP MQWs layer (~ 180 nm thick) located ~100 nm from the bottom of the device (i.e., the Ge/Au layer). Figure 5e,f shows the angle-resolved PL spectra of the device when pumping below (e) and above (f) lasing threshold (see supplementary Fig. S12 for the PL spectra of other devices, out of which only that with W = 110 nm can achieve lasing). It is noted that the lasing threshold for this device is ~ 350 μJ/cm^2, which is > 2 times higher than that of the array with t_{slab} = 300 nm and W = 90 nm as shown in Figure 2 (i.e., lasing threshold = 150 μJ/cm^2). This can be explained by the poorer overlapping between the higher order mode profiles and the gain medium (i.e., only a portion of the field is within the MQW layer). As we can see, above lasing threshold, multiple well-defined beams emitted at different angles and wavelengths can be obtained. Figure 5g shows the lasing spectra at different angles extracted from Fig. 5f. It can be noted that the quality factors of the laser beams decrease with higher angle lasing modes. While the Q-factor of both BIC modes (i.e., Symmetry-protected and accidental) is of the same value for an infinite system (infinite for lossless case, limited by the metal electrode absorption in ours), for a finite-sized system, one should expect a lower Q-factor due to the loss of transversed-wave leakage. In this case, the leakage is expected to be more severe for the off-Gamma points (i.e., accidental BICs) leading to a lower Q factor of the modes.. Figure 5h shows the normalized-intensity lasing directionality for different modes. It can be seen that lasing beams at four different wavelengths emit at discrete angles with ~ 2.5° separation between them. Figure 5i shows the BFP image of the lasing emission, indicating both symmetry-protected BIC (near 0° angle) and accidental BIC emission (at oblique angles). It is interesting to note that the line-like lasing patterns can be seen for both symmetry-protected and accidental BIC modes.

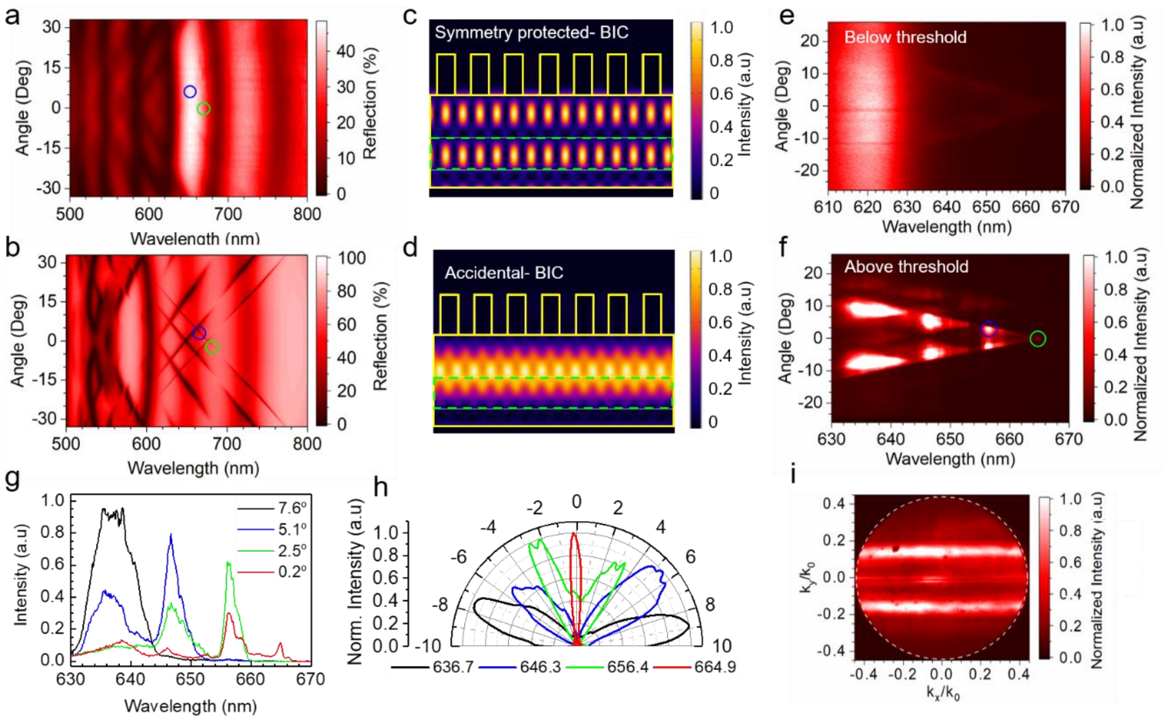

Figure 5. (a), (b) Measured and simulated reflection spectra for TM excitation of a device with a slab thickness t = 570 nm, a grating height h= 250 nm and a grating beam width W = 110 nm (i.e., P = 210 nm). The green and blue circles indicate the location of a symmetry-protected and an accidental BIC, respectively. (c), (d) Field distribution within the cavity structure for the case of symmetry-protected and accidental BIC, respectively. (e), (f) Angle-resolved PL spectra below (e) and above (f) lasing threshold. (g) Lasing spectra at different angles, showing four distinct lasing modes at 664.9 nm (symmetry-protected BIC) and 656.4, 646.4, 636.7 nm (accidental BICs). (h) Normalized angular distribution of radiation at the four different lasing wavelengths showing multi-beam profiles of the lasing signals. (i) BFP image of the PL above lasing threshold showing distinct lasing beams of both symmetry-protected and accidental BIC modes.

In summary, we have shown a way to design a laser cavity with controllable directionality and lasing wavelength. By using the BICs formed by destructive interference between counter-propagating guided modes, high quality-factor cavities can be designed. We experimentally demonstrated this laser concept using a standard industrial III-V semiconductor platform and achieved room-temperature lasing action for both single-mode and multi-beam, multi-wavelength laser devices. The resulting lasers have a very high polarization degree and well-defined emission directionality. We believe this work is an important stepping stone in laser cavity design and will expand the toolbox for multi-functional, miniaturized light sources, which may find many applications in optical communications, bio-sensing and other advanced optoelectronic devices.

METHODS

Nanofabrication of the laser device

GaP LED wafer with Ge/Au layers on silicon substrate was purchased from ChangeLight Co., Ltd (China). The 4-inch wafer was rinsed with acetone, IPA, and DI water and blown with dried nitrogen gas before cutting into smaller coupons with the size of 1×1 cm^2 by a diamond pen. The thickness of the device layer (GaP-based layers above Ge/Au) was monitored by reflectometry (Filmmetric® F20). The model used to calculate the device film thickness was verified by SEM measurements of the cross-section of the same device. The sample was etched by reactive ion etching (Oxford Plasmalab 100) using Cl_2 and N_2 as the reaction gases at 200°C to the desired device thickness (i.e., slab layer thickness + grating height). Electron beam lithography (Elionix 7000) was used to pattern grating structures on n-AlInP layer using hydrogen silsesquioxane (HSQ - XR-1541-006, Dow Corning) as a negative resist. The grating structures were then transferred into n-AlInP by the same dried-etching process to achieve a desired depth of the grating.

Optical characterization

Angle-resolved reflection and photoluminescence measurements were performed on a home-built micro-spectrometer setup. The system consists of an inverted optical microscope (Nikon Ti-U) with a suitable colour filter set (i.e., Dichroic mirror and filters), a spectrograph (Andor SR-303i) equipped with different grating plates (150 lines/mm for broadband reflection measurement, and 1200 lines/mm for high spectral resolution lasing measurement), and a two-dimensional (1600 × 400) electron-multiplying charged-coupled detector (EMCCD, Andor Newton 971) connected to one of the output ports of the spectrograph. A lens system along the light path between the microscope and the spectrograph was used to project either the imaging plane or back focal plane of the collection objective onto the slit of the spectrograph. The back focal plane configuration yielded angle-resolved spectroscopic measurements. For reflectance measurements, the excitation light from a halogen lamp was focused on the device area using a 50× microscope objective with a numerical aperture (NA) of 0.55 (Nikon). A linear polarizer placed in the path of the light source was used to control the excitation polarization. For lasing measurement, a Ti-sapphire femtosecond laser system (Coherent® Mira 900) equipped with an optical parametric amplifier (OPA- Coherent® Reg A) was used to produce an excitation wavelength of 530 nm with a pulse duration of 200 fs and pulse repetition rate of 20 kHz. All optical measurements were performed at ambient conditions.

Numerical Simulations

Angle-resolved reflection and mode profile distribution simulations were done using the Finite Element Method (Comsol Multiphysics v5.5). For that, a single unit cell was simulated, and Bloch boundary conditions were applied in the lateral directions to mimic an infinite system. This system was excited, and the reflection was recorded using a set of periodic ports.The material parameters used are those corresponding to the experimental data of the built-in Optical Material Library.

ASSOCIATED CONTENT

Supplementary information

Cross-section of the GaP wafer; schematic of the laser device fabrication process; simulated and experimentally measured angle-resolved reflectance spectra and PL spectra of devices with various grating parameters and slab thicknesses.

AUTHOR INFORMATION

Corresponding Author

*Email: arseniy_kuznetsov@imre.a-star.edu.sg

Author Contributions

R.P.D. conceived the idea of this work. S.T.H. fabricated the samples, measured reflection, lasing, SEM and wrote the first draft of the manuscript. R.P.D. performed the numerical simulations and theoretical analysis. A.I.K. supervised the project. All authors discussed the data and contributed to the writing of the manuscript.

Notes

The authors declare no competing financial interest.

ACKNOWLEDGEMENTS

This work was supported by the A*STAR SERC Pharos programme (grant number 152 73 00025) and MTC Programmatic Grant No. M21J9b0085.

The authors acknowledge Dr. Wong Seng Kai (IMRE, A*STAR) for FIB/SEM characterization of the device cross-section.

TOC graphic

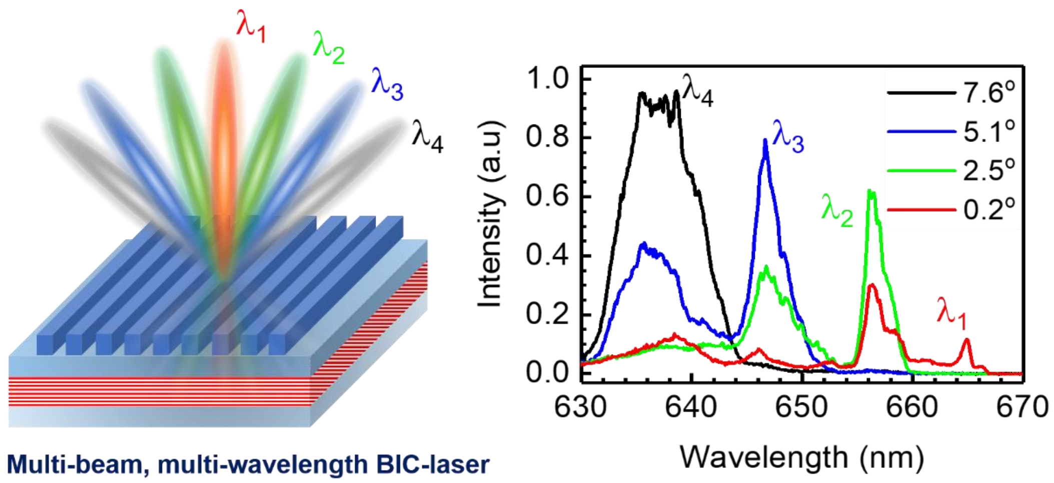

REFERENCES

1. Zhan, X. *et al.* 3D Laser Displays Based on Circularly Polarized Lasing from Cholesteric Liquid Crystal Arrays. *Advanced Materials* **33**, (2021).
2. Liang, J., Chu, M., Zhou, Z., Yan, Y. & Zhao, Y. S. Optically Pumped Lasing in Microscale Light-Emitting Electrochemical Cell Arrays for Multicolor Displays. *Nano Letters* **20**, (2020).
3. Zhao, J. *et al.* Full-color laser displays based on organic printed microlaser arrays. *Nature Communications* **10**, (2019).
4. Uchida, A. *et al.* Fast physical random bit generation with chaotic semiconductor lasers. *Nature Photonics* **2**, (2008).
5. Sun, Y. *et al.* Room-temperature continuous-wave electrically injected InGaN-based laser directly grown on Si. *Nature Photonics* **10**, (2016).
6. Roelkens, G. *et al.* III-V/silicon photonics for on-chip and intra-chip optical interconnects. *Laser and Photonics Reviews* **4**, (2010).
7. Chen, R. *et al.* Nanolasers grown on silicon. *Nature Photonics* **5**, (2011).
8. Zhou, Z., Yin, B. & Michel, J. On-chip light sources for silicon photonics. *Light: Science and Applications* vol. 4 (2015).
9. Toropov, N. *et al.* Review of biosensing with whispering-gallery mode lasers. *Light: Science and Applications* vol. 10 (2021).
10. Deng, H., Lippi, G. L., Mørk, J., Wiersig, J. & Reitzenstein, S. Physics and Applications of High-β Micro- and Nanolasers. *Advanced Optical Materials* vol. 9 (2021).
11. Deka, S. S., Jiang, S., Pan, S. H. & Fainman, Y. Nanolaser arrays: Toward application-driven dense integration. *Nanophotonics* vol. 10 (2021).
12. Miao, P. *et al.* Orbital angular momentum microlaser. *Science (1979)* **353**, (2016).
13. Fan, F., Turkdogan, S., Liu, Z., Shelhammer, D. & Ning, C. Z. A monolithic white laser. *Nature Nanotechnology* **10**, (2015).
14. Lindemann, M. *et al.* Ultrafast spin-lasers. *Nature* **568**, (2019).
15. Hirose, K. *et al.* Watt-class high-power, high-beam-quality photonic-crystal lasers. *Nature Photonics* **8**, (2014).

16. Jeong, K. Y. *et al.* Recent Progress in Nanolaser Technology. *Advanced Materials* **32**, (2020).
17. Rauter, P. & Capasso, F. Multi-wavelength quantum cascade laser arrays. *Laser and Photonics Reviews* **9**, (2015).
18. Yu, N. *et al.* Multi-beam multi-wavelength semiconductor lasers. *Applied Physics Letters* **95**, (2009).
19. Molina, M. I., Miroshnichenko, A. E. & Kivshar, Y. S. Surface bound states in the continuum. *Physical Review Letters* **108**, (2012).
20. Marinica, D. C., Borisov, A. G. & Shabanov, S. v. Bound states in the continuum in photonics. *Physical Review Letters* **100**, (2008).
21. Azzam, S. I. & Kildishev, A. v. Photonic Bound States in the Continuum: From Basics to Applications. *Advanced Optical Materials* vol. 9 (2021).
22. Friedrich, H. & Wintgen, D. Interfering resonances and bound states in the continuum. *Physical Review A* **32**, (1985).
23. Sadrieva, Z., Frizyuk, K., Petrov, M., Kivshar, Y. & Bogdanov, A. Multipolar origin of bound states in the continuum. *Physical Review B* **100**, (2019).
24. Plotnik, Y. *et al.* Experimental observation of optical bound states in the continuum. *Physical Review Letters* **107**, (2011).
25. Zhen, B., Hsu, C. W., Lu, L., Stone, A. D. & Soljačić, M. Topological nature of optical bound states in the continuum. *Physical Review Letters* **113**, (2014).
26. Koshelev, K., Bogdanov, A. & Kivshar, Y. Meta-optics and bound states in the continuum. *Science Bulletin* vol. 64 (2019).
27. Ovcharenko, A. I., Blanchard, C., Hugonin, J. P. & Sauvan, C. Bound states in the continuum in symmetric and asymmetric photonic crystal slabs. *Physical Review B* **101**, (2020).
28. Yang, Y., Peng, C., Liang, Y., Li, Z. & Noda, S. Analytical perspective for bound states in the continuum in photonic crystal slabs. *Physical Review Letters* **113**, (2014).
29. Doeleman, H. M., Monticone, F., den Hollander, W., Alù, A. & Koenderink, A. F. Experimental observation of a polarization vortex at an optical bound state in the continuum. *Nature Photonics* **12**, (2018).
30. Kodigala, A. *et al.* Lasing action from photonic bound states in continuum. *Nature* **541**, (2017).
31. Midya, B. & Konotop, V. v. Coherent-perfect-absorber and laser for bound states in a continuum. *Optics Letters* **43**, (2018).
32. Hwang, M. S. *et al.* Ultralow-threshold laser using super-bound states in the continuum. *Nature Communications* **12**, (2021).
33. Yu, Y. *et al.* Ultra-coherent Fano laser based on a bound state in the continuum. *Nature Photonics* **15**, (2021).
34. Yang, J. H. *et al.* Low-Threshold Bound State in the Continuum Lasers in Hybrid Lattice Resonance Metasurfaces. *Laser and Photonics Reviews* **15**, (2021).
35. Wu, M. *et al.* Bound State in the Continuum in Nanoantenna-Coupled Slab Waveguide Enables Low-Threshold Quantum-Dot Lasing. *Nano Letters* **21**, (2021).
36. Ha, S. T. *et al.* Directional lasing in resonant semiconductor nanoantenna arrays. *Nature Nanotechnology* **13**, (2018).
37. Mylnikov, V. *et al.* Lasing Action in Single Subwavelength Particles Supporting Supercavity Modes. *ACS Nano* **14**, (2020).

38. Wang, Y. *et al.* Highly Controllable Etchless Perovskite Microlasers Based on Bound States in the Continuum. *ACS Nano* **15**, (2021).
39. Huang, C. *et al.* Ultrafast control of vortex microlasers. *Science (1979)* **367**, (2020).
40. Tian, J. *et al.* Phase-change perovskite tunable microlaser. *arXiv* (2021).
41. Azzam, S. I. *et al.* Single and Multi-Mode Directional Lasing from Arrays of Dielectric Nanoresonators. *Laser and Photonics Reviews* **15**, (2021).
42. Monticone, F. & Alù, A. Bound states within the radiation continuum in diffraction gratings and the role of leaky modes. *New Journal of Physics* **19**, (2017).
43. Quaranta, G., Basset, G., Martin, O. J. F. & Gallinet, B. Recent Advances in Resonant Waveguide Gratings. *Laser and Photonics Reviews* vol. 12 (2018).
44. Bykov, D. A., Bezus, E. A. & Doskolovich, L. L. Coupled-wave formalism for bound states in the continuum in guided-mode resonant gratings. *Physical Review A* **99**, (2019).
45. Sadrieva, Z. F. *et al.* Transition from Optical Bound States in the Continuum to Leaky Resonances: Role of Substrate and Roughness. *ACS Photonics* **4**, (2017).
46. Zihao, C. *et al.* Analytical theory of finite-size photonic crystal slabs near the band edge. *Optics Express* **30**, 14033–14047 (2022).
47. Sakai, K. *et al.* Lasing band-edge identification for a surface-emitting photonic crystal laser. *IEEE Journal on Selected Areas in Communications* **23**, (2005).
48. Ying, C. F., Zhou, W. Y., Ye, Q., Zhang, X. L. & Tian, J. G. Band-edge lasing in Rh6G-doped dichromated gelatin at different excitations. *Journal of Optics* **12**, (2010).
49. Cho, C. O. *et al.* Photonic crystal band edge laser array with a holographically generated square-lattice pattern. *Applied Physics Letters* **87**, (2005).
50. Zhou, W. *et al.* Lasing action in strongly coupled plasmonic nanocavity arrays. *Nature Nanotechnology* **8**, (2013).